# Characterization of strain-induced martensitic transformation in a metastable austenitic stainless steel

P. Haušild [a,*], V. Davydov [b,c], J. Drahokoupil [c,d], M. Landa [e], P. Pilvin [f]

[a] *Department of Materials, Faculty of Nuclear Sciences and Physical Engineering, Czech Technical University in Prague, Trojanova 13, 120 00 Praha 2, Czech Republic*
[b] *Department of Neutron Physics, Nuclear Physics Institute, Academy of Sciences of the Czech Republic, 250 68 Řež, Czech Republic*
[c] *Department of Solid State Engineering, Faculty of Nuclear Sciences and Physical Engineering, Czech Technical University in Prague, Trojanova 13, 120 00 Praha 2, Czech Republic*
[d] *Institute of Physics, Academy of Sciences of the Czech Republic, Na Slovance 2, 18221 Prague 8, Czech Republic*
[e] *Institute of Thermomechanics, Academy of Sciences of the Czech Republic, Dolejškova 5, 182 00 Praha 8, Czech Republic*
[f] *Laboratoire d'Ingénierie des Matériaux de Bretagne, Université de Bretagne-Sud, Rue de Saint Maudé, BP 92116, 56321 Lorient, France*

## ARTICLE INFO

## ABSTRACT

Kinetics of deformation-induced martensitic transformation in metastable austenitic steel AISI 301 was characterized by several techniques including classical light metallography, scanning electron microscopy, X-ray diffraction, neutron diffraction and electron back scattered diffraction. *In situ* monitoring of magnetic properties, acoustic emission and temperature increase during tensile tests at different strain rates was also performed. Results obtained by different methods are compared and discussed.

© 2009 Elsevier Ltd. All rights reserved.

## 1. Introduction

During the cold forming process, low nickel austenitic stainless steels can undergo plastic deformation-induced phase transformation of face-centered cubic (fcc) $\gamma$ austenite to hexagonal closed packed (hcp) $\varepsilon$-martensite and body-centered cubic (bcc) $\alpha'$-martensite [1]. $\varepsilon$-martensite forms from randomly spaced overlapping stacking faults and $\alpha'$-martensite forms at shear band intersections [2–4]. High stacking fault energy (>20 mJ m$^{-2}$) promote direct transformation $\gamma \rightarrow \alpha'$, low stacking fault energy (<20 mJ m$^{-2}$) leads to the transformation $\gamma \rightarrow \varepsilon \rightarrow \alpha'$ [5].

The $\gamma \rightarrow \alpha'$ transformation increases the strain hardening rate [6]. High internal stresses are generated due to an incompatible transformation strain accompanying the martensitic transformation (shear strain of 20% can cause a volume change of 2% [7]). A good knowledge of martensitic transformation kinetics is therefore an essential constituent for good control of the forming process.

There are several non-destructive techniques which can be used in order to characterize the martensite volume fraction. Intrinsic electromagnetic properties are obviously suitable to characterize the phase transformation of the non-magnetic phase (austenite) to the magnetic one ($\alpha'$-artensite) [8–10]. Corresponding changes of magnetic properties can be detected by measuring the eddy current impedance, the magnetic permeability and the remanence field [11–14]. However, it is not trivial to relate directly the mag-

netic properties to the volume fraction of deformation-induced $\alpha'$-artensite. Bloch walls are temporarily pinned by the lattice defects induced by strain hardening [12]. A further increase in magnetic field strength is needed to overcome the pinning effect and to increase magnetization. The overall magnetization behavior is therefore strongly influenced by the density of the pinning points, i.e., the density of the lattice defects. Obviously, non-magnetic $\varepsilon$-martensite cannot be detected by magnetic methods.

Sudden local rearrangement of the internal stress field produced by rapid events such as twinning or microcracking can generate acoustic emission (AE) [15–17]. AE generated by martensitic transformation has already been monitored (e.g., in Fe–Ni–C alloy [18]).

For accurate evaluation of martensite volume fraction, it is required to use diffraction methods (X-ray, electron, neutron). For non-textured materials, the phase volume fraction is deduced from peak intensities of each phase. For the material which develops crystallographic texture, it is necessary to rectify the peak intensities changed by the preferred orientation. In addition to initial texture, the transformation texture arises because not all possible crystallographic variants grow when the austenite is subjected to external stress; i.e., the total number of selected variants within a $\gamma$-grain is much lower than 24 which are theoretically allowed by the Kurdjumov–Sachs orientation relations [4].

The aim of this paper is to compare the characterization of martensitic transformation in metastable austenitic steel by several techniques including classical light metallography, scanning electron microscopy (SEM), X-ray diffraction, neutron diffraction and

---

* Corresponding author. Tel.: +420 224358514; fax: +420 224358523.
*E-mail address:* Petr.Hausild@fjfi.cvut.cz (P. Haušild).

**Table 1**
Chemical composition of AISI 301 steel (in wt.%).

|  | C | Cr | Ni | Si | Mn | Mo |
|---|---|---|---|---|---|---|
| Nominal | Max 0.12 | 16–18 | 6.5–9 | <1.5 | <2 | <0.8 |
| Analyzed | 0.05 | 17 | 7 | 0.5 | 1.5 | 0.1 |

**Table 2**
Results of tensile tests at room temperature for different applied strain rates.

| Strain rate ($s^{-1}$) | 0.2% Proof stress (MPa) | Ultimate tensile strength (MPa) | Elongation (%) |
|---|---|---|---|
| $5 \times 10^{-5}$ | 270 | 912 | 20 |
| $5 \times 10^{-4}$ | 288 | 905 | 24 |
| $5 \times 10^{-3}$ | 308 | 895 | 34 |
| $5 \times 10^{-2}$ | 324 | 866 | 31 |

electron back scattered diffraction (EBSD). Monitoring of magnetic properties, acoustic emission and temperature during tensile tests was also performed.

## 2. Material

The material chosen for this paper was experimental steel provided by the ARCELOR-MITTAL. The chemical composition is given in Table 1 and corresponds to the AISI 301 grade. The low nickel and chromium content situates the steel at the limit of the austenite field in the Schaeffler's diagram [19]. The formula proposed by Scharam and Reed [20] yields a stacking fault energy value of ∼8 mJ m$^{-2}$. The material was supplied as cold rolled sheets of 0.68 mm thickness in the bright annealed state.

The tensile tests were carried out on an INSPEKT 100 kN testing machine at room temperature imposing various strain rates ranging from $\dot{\varepsilon} = 5 \times 10^{-5}$ s$^{-1}$ to $\dot{\varepsilon} = 5 \times 10^{-2}$ s$^{-1}$. All tests were repeated at least twice (including those with the *in situ* monitoring) in order to assure the repeatability and reproducibility of results.

Tensile properties at room temperature obtained with strain rates ranging from $\dot{\varepsilon} = 5 \times 10^{-5}$ s$^{-1}$ to $\dot{\varepsilon} = 5 \times 10^{-2}$ s$^{-1}$ are listed in Table 2. A distinct change in the slope of stress–strain curves (increase of the hardening rate) occurred due to the presence of the deformation-induced martensitic phase.
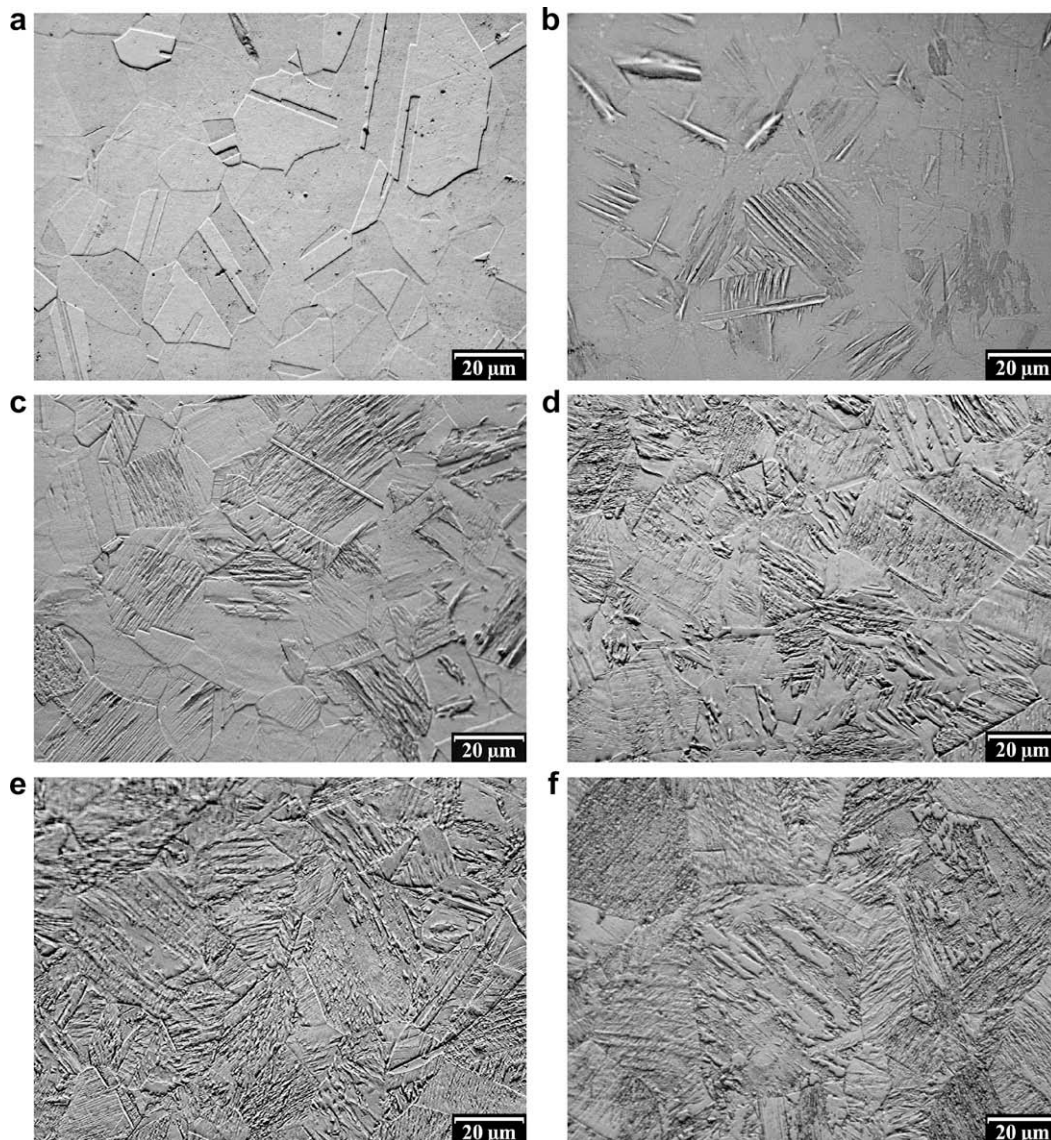


**Fig. 1.** Microstructure of AISI301 steel in (a) non-deformed state (and after different tensile pre-deformation, (b) 2.5%, (c) 5%, (d) 10%, (e) 15% and (f) 20% of true equivalent plastic strain (light microscopy).

The shape of stress–strain curves is strongly dependent on strain rate. With increasing strain rate yield stress increases, ultimate tensile strength decreases and elongation to fracture has a maximum at $\dot{\varepsilon} = 5 \times 10^{-3}\,\mathrm{s}^{-1}$. During the tests at higher strain rates ($\dot{\varepsilon} = 5 \times 10^{-3}\,\mathrm{s}^{-1}$ and $\dot{\varepsilon} = 5 \times 10^{-2}\,\mathrm{s}^{-1}$), the heating of specimens occurred.

In order to characterize martensitic transformation, several specimens were tensile pre-deformed up to 20% of true (logarithmic) equivalent plastic strain and compared with non-deformed state. Strain rate for tensile pre-deformation was chosen $\dot{\varepsilon} = 5 \times 10^{-4}\,\mathrm{s}^{-1}$ in order to avoid the heating of specimens.

## 3. Experimental techniques

### 3.1. Metallography

In metastable steels, mechanical grinding and polishing can produce deformation-induced martensitic transformation in the surface layer. In order to avoid this effect, electro-polishing in 5% perchloric acid solution in ethanol was carried out at 40 V.

Microstructure was revealed by etching in 1:1:1 solution of $H_2O$, HCl and $HNO_3$. The samples were observed using the Neophot 32 light optical microscope and the scanning electron microscope JSM 840. SEM observations were performed at 25 kV. The micrographs were recorded at normal incidence.

### 3.2. Diffraction methods

#### 3.2.1. X-ray diffraction

The X-ray diffraction measurement was performed on X'Pert PRO diffractometer with a sample stage for texture analysis ATC-3, Co anode (wavelength $\lambda = 0.1789$ nm) and X'Celerator detector. The penetration depth of X-rays (Co radiation) to steel is a few micrometers. The analyzed area was 4–24 mm$^2$ (depending on diffraction and inclination angles).

The determination of $\alpha'$-martensite phase content was carried out by the method corresponding to a simplified multiphase Rietveld analysis, i.e., the average intensities of pole figures $I_p^{avrP}$ were compared (instead of comparison of every point in the diffraction pattern). The pole figures of austenite lines ($\langle 1\,1\,1\rangle$, $\langle 2\,0\,0\rangle$, $\langle 2\,2\,0\rangle$, $\langle 3\,1\,1\rangle$, $\langle 2\,2\,2\rangle$) and $\alpha'$-martensite lines ($\langle 1\,1\,0\rangle$, $\langle 2\,0\,0\rangle$, $\langle 2\,1\,1\rangle$, $\langle 2\,2\,0\rangle$) were measured in the range of angles $\psi$ from 0° to 80°, $\varphi$ from 0° to 360°, both angles with steps of 10° (Fig. 3). X'Pert Texture software was used to compute the orientation distribution function and full pole figures. Background and defocusing correction was used.

The scale factors of individual phases were computed by the minimization of R factor given by formula (1):

$$R = \frac{\sum_p w_p (I_p^{avrP} - I_p^{cal})^2}{\sum_p w_p (I_p^{cal})^2} \tag{1}$$

where $w_p = \frac{1}{I_p^{avrP}}$ are weight factors, $p$ is the diffraction peak of martensite or austenite, calculated intensity for particular diffraction $I_p^{cal} = mSLPF$, $m$ the multiplicity factor, $S$ the scale factor, $L$ the Lorentz factor, $P$ the polarization factor and $F$ is the structure factor. A more detailed description of computing the intensity of diffraction peaks could be found, e.g., in [21]. The weight fractions were computed from refined scales factors according to formula (2) [22].

$$W_\alpha = \frac{(SZMV)_\alpha}{\sum_i (SZMV)_i} \tag{2}$$

where $S$ is the scale factor, $Z$ the number of formula units per unit cell ($Z_\gamma = 4$, $Z_\varepsilon = 2$, $Z_{\alpha'} = 2$), $M$ the mass of the formula unit ($M = 55.847$ g mol$^{-1}$) and $V$ is the unit cell volume ($V_\gamma = 0.0478$ nm$^3$, $V_\varepsilon = 0.021$ nm$^3$, $V_{\alpha'} = 0.0236$ nm$^3$). Lattice parameters are $a = 0.363$ nm for austenite; $a = 0.287$ nm for $\alpha'$-martensite; $a = 0.254$ nm and $c = 0.416$ nm for $\varepsilon$-martensite.

The uncertainties in phase content given by this fitting procedure are approximately ±3% for 95% confidence interval.

#### 3.2.2. Neutron diffraction

The neutron diffraction experiment was performed at a multi-purpose neutron diffractometer TEXTDIFF located at the Neutron Physics Laboratory at a steady state reactor LVR-15 in Řež. A horizontally bent Si-crystal produced the monochromatic beam of neutrons with wavelength $\lambda = 0.16476$ nm. The diffraction measurements were conducted in the continuous $2\theta/\theta$ step-scan mode with an angular step size 0.1° of point-detector ($^3$He). The $2\theta$ angular working range of diffractometer was from 10° to 110°.

Square strips $10 \times 10$ mm$^2$ were cut from the specimens with the same level of tensile pre-deformation and assembled into 5-layer stacks in order to increase the sampled volume. So prepared samples were bathed in the neutron beam during the measurements in order to obtain information on individual phases from the whole volume and thus to eliminate possible statistical errors connected with partially irradiated specimen.

For quantitative determination of the phase content, the neutron diffraction data were analyzed by Rietveld refinement method using the FullProf-suite software [23]. The full pattern decomposition technique was used, which is fundamentally biased by the chosen unit cell dimensions of phases present. In this case, the peak positions (Fig. 4) are defined by the unit cell dimensions, where the reflection intensities are established by the distribution of atoms in the unit cell of every crystalline phase present in the sample. This method relies on fitting the whole powder pattern at once [21]. The integrated intensities are, however, determined individually for each Bragg reflection.

In the Rietveld analysis, several parameters were carefully refined including the phase scale factors and the background component of the patterns, the lattice parameters, the $2\theta$ zero point offset,
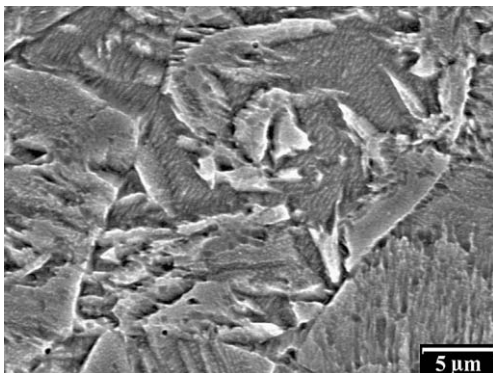


**Fig. 2.** Martensite in AISI 301 steel after tensile pre-deformation to 20% of true equivalent plastic strain (scanning electron microscopy).
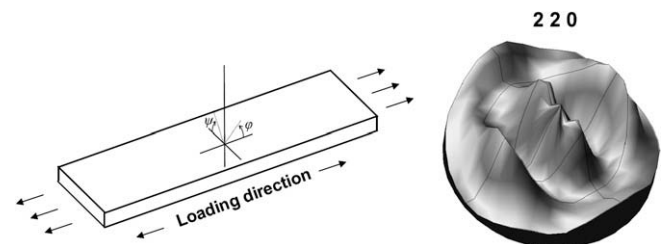


**220**

**Fig. 3.** (2 2 0) pole figure of austenite after tensile pre-deformation to 10% of true equivalent plastic strain (X-ray).
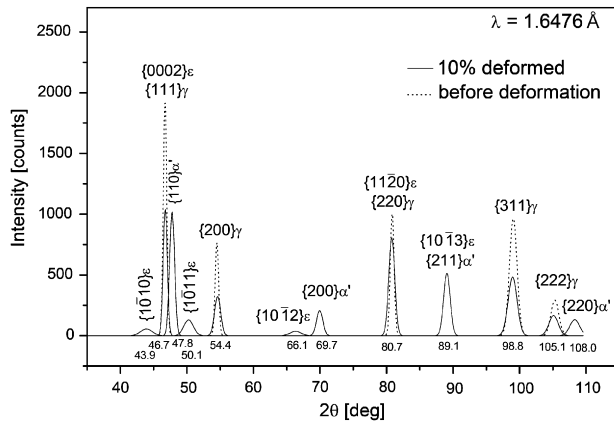
**Fig. 4.** Rietveld refinement of neutron diffraction pattern for sample before and after tensile pre-deformation to 10% of true equivalent plastic strain.

the parameters of the pseudo-Voigt profile functions and aniso-tropic strain parameters [24] for each phase, and preferred orientations.

Since the magnetic contributions to the nuclear Bragg intensities were neglected in the Rietveld analyses because of the very low ferromagnetic components [25,26], only the texture components needed to be corrected. The elimination of texture was performed in the Rietveld analysis by using March's function, adapted to both fiber and platy habits [23]. The uncertainties in the phase content determined by Rietveld refinement were less than ±2% for each phase.

### 3.2.3. Electron back scattered diffraction

EBSD analysis was carried out in scanning electron microscope FEI Quanta 200 FEG equipped with a TSL™ EBSD analyzer. The electropolished samples were inspected at a tilt angle of 70°. Acquired data were evaluated by OIM™ software.

Several conditions, especially the size of the analyzed area and the size of the beam spot, were used in order to assure the reproducibility of analysis. The analyzed area should be sufficiently large for good statistics, which can simultaneously increase time of analysis and exacerbate the focusing conditions. The most frequently used size of the analyzed area was $300 \times 300 \ \mu m^2$ (approximately 100 primary austenitic grains).

EBSD technique is principally utilized for automatic determination (mapping) of local crystal structure and crystallographic orientation. Angles between each pair of Kikuchi lines (identified using Hough transform) are compared with a table of so called

interzonal angles (characteristic for each crystal structure) in order to assign the orientation to Kikuchi pattern. Since not all the lines are detected, a multivalent solution exists. A choice of orientation is then made by a vote scheme. The phase identification is generally correct when the confidence index (i.e., difference between votes for the first and second solution divided by the total possible number of votes corresponding to the detected pattern) is high. For low confidence index pattern, phase assessment can be uncertain and can lead to an error in the volume fraction ranging from few percents to tens of percent. Better solution is independent identification of each phase and elimination of low confidence results (e.g., CI < 0.1 for austenite, CI < 0.15 for α′-martensite and ε-martensite, see Fig. 5). If there is no overlapping, then the upper and lower limit of martensite volume fraction can be estimated.

### 3.3. In situ measurements

#### 3.3.1. Magnetic measurement

Phase transformation of the non-magnetic phase (austenite) to the magnetic one (α′-martensite) during the tensile test was characterized using the magnetic induction method. The Fischer FERIT-SCOPE® MP30 device was used for this purpose. In this measuring system, low frequency alternating magnetic field generated by the first (excitation) coil interacts with the magnetic phase in the specimen. The changes in the magnetic field induce voltage in the second (measuring) coil. This voltage is proportional to the martensite content.

#### 3.3.2. Acoustic emission

The AE signal was monitored during selected tensile tests using a highly sensitive transducer coupled to the specimen head. A computer controlled DAKEL-XEDO-6 AE facility was used to record the AE counts. The AE facility applied a two threshold level system of detection and evaluation of AE, recently recommended by an ASTM standard. The lower threshold level was 556 mV, the higher threshold level was 1200 mV. The total gain was about 100 dB.

#### 3.3.3. Thermal analysis

Temperature increase during the tensile tests was measured by a chromel–alumel thermocouple connected with the PC via Omegaette HH306 data logger and ThermoLog software.

## 4. Results and discussion

### 4.1. Metallography

Fig. 1 shows the microstructure in non-deformed state (as received) and after 2.5%, 5%, 10%, 15% and 20% of plastic deformation.
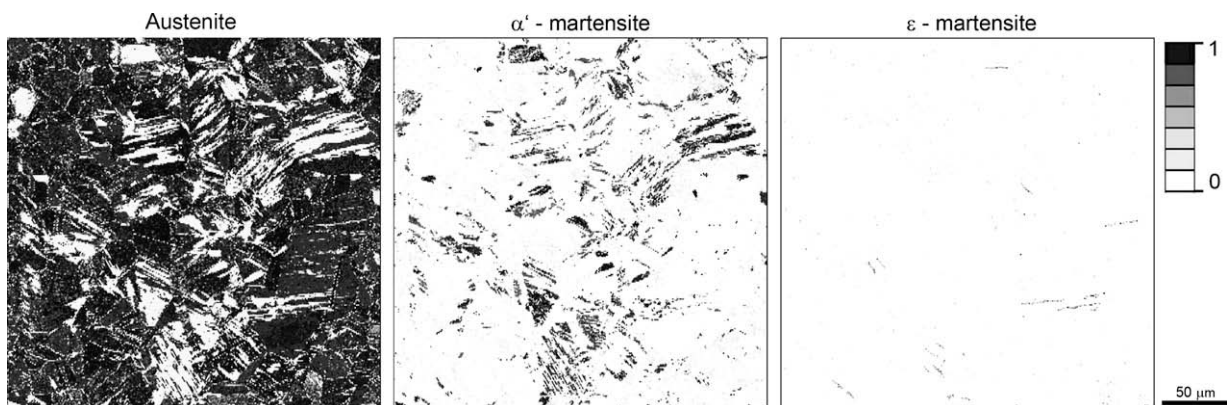


**Fig. 5.** Confidence index of different phases in AISI 301 steel after tensile pre-deformation to 5% of true equivalent plastic strain (EBSD).

In non-deformed state, the microstructure is composed of equi-axed austenitic grains with typical annealing twins. After 2.5% of plastic deformation, several martensitic variants can be seen inside the austenitic grains. After 20% of plastic deformation, the micro-structure is mostly martensitic (Fig. 2). Light microscopy was per-formed using bright field with slightly inclined illumination to increase the contrast. Differential phase contrast can also be effec-tively used to visualize the deformed microstructure.

However, classical light or scanning electron microscopy do not allow us to distinguish precisely between martensitic lathes, slip lines and deformation twins and to quantify the martensitic vol-ume fraction by image analysis.

### 4.2. Diffraction methods

Martensite volume fractions obtained by EBSD, X-ray and neu-tron diffraction are compared in Figs. 6 and 7. A fairly good agree-ment in $\alpha'$-martensite volume fraction was obtained by all methods employed.

The volume fraction of deformation-induced $\alpha'$ martensite, $f_m$, can be effectively described by the kinetics equation [27]:

$$f_m = 1 - \exp(-\beta\varepsilon_{pl}^n) \tag{3}$$

where $\varepsilon_{pl}$ is the plastic strain, $\beta$ is the stability parameter and $n$ is the deformation mode parameter.

The contribution of peaks characteristic for $\varepsilon$-martensite was very weak in the X-ray diffraction spectra (i.e., comparable to the precision of the method) so that the volume fraction of $\varepsilon$-martens-ite was neglected and only austenite and $\alpha'$-martensite volume fractions were determined. Just the lower bound of $\varepsilon$-martensite volume fraction can be reliably obtained by EBSD, and only neu-tron diffraction yielded the values with reasonable error.

A comparative neutron diffraction macrotexture analysis cor-roborated the existence of preferred orientations determined by Rietveld analysis. The most distinct (1 1 1) fiber texture component was observed in austenitic phase along the loading direction [28], which became more intensive with the increased level of applied plastic deformation. Different behavior of texture was revealed in $\alpha'$-martensitic phase; here several preferred orientations varied in the whole deformation range. The detailed macrotexture analy-sis will be presented elsewhere.

Even if the neutron diffraction method is very accurate in quan-titative analysis of $\alpha'$-martensite and $\varepsilon$-martensite volume frac-tions determined from the whole volume of studied specimens, this technique has some limitations. The time of collecting of spec-tra has to be increased as the volume fraction of present phase de-creases, in order to enlarge integral intensity and thus to diminish
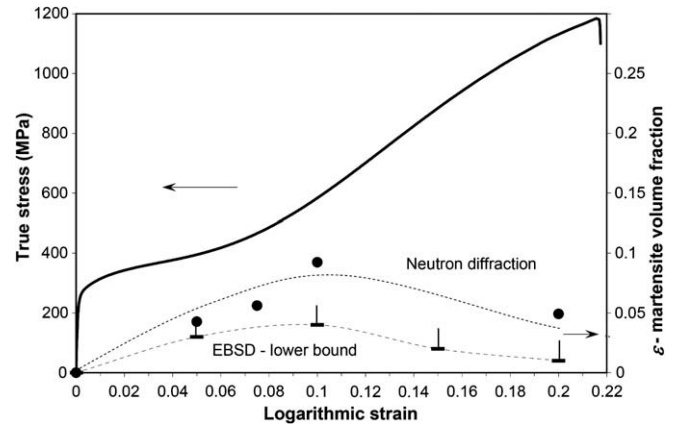


**Fig. 7.** Evolution of $\varepsilon$-martensite volume fraction after tensile deformation.

uncertainties of further refinement procedure. As well, the angular resolution of diffractometer is decreasing as Bragg angle ap-proaches the backscattering geometry ($2\theta = 180°$). This becomes apparent in diffraction peak broadening which occur with a para-bolic dependency.

EBSD analysis showed higher scatter which could partially be due to the smaller area analyzed. Also, another source of error may be various surface qualities in different phases (after polish-ing) and different confident index thresholds in each phase (to avoid the phase overlapping). The main advantage of EBSD tech-nique is that it gives local information. It can be used even in the case when X-ray diffraction fails, e.g., due to coarse grains. It brings 3D orientation but only on the surface (spatial resolution for $\alpha$-iron and field emission gun is about 10 nm [29]) and do not take into account 3D geometry of microstructure. Especially in the case of bainite or martensite, sectioning effects can lead to the variant selection, i.e., variants having their long axis closest to sectioning plane have high apparent fraction [30].

### 4.3. Magnetic measurement

It is not trivial to relate directly the magnetic properties to the volume fraction of deformation-induced martensite. Very different (shifted) results are obtained measuring in the loaded (under stress) and unloaded (zero stress) state. The geometry of the mea-sured piece (thickness, curvature, etc.) can also play an important role. The results must be therefore calibrated. In our case, we used for calibration the results of diffraction methods (see Fig. 6).
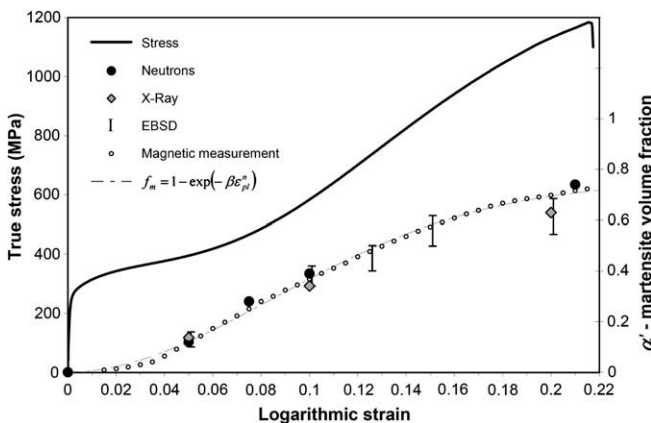


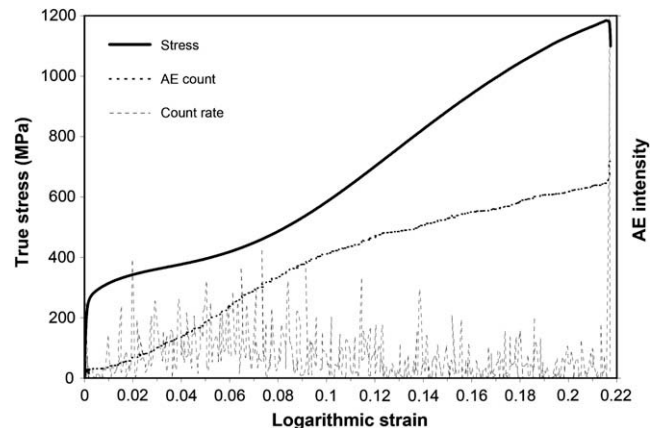**Fig. 6.** Evolution of $\alpha'$-martensite volume fraction after tensile deformation.



**Fig. 8.** AE during the tensile test of AISI 301 steel tested at room temperature at $\dot{\varepsilon} = 5 \times 10^{-4}\,\mathrm{s}^{-1}$.

Better results can be obtained by measuring the saturation conditions, nevertheless strong magnetic field ($H \sim 2T$) must be then generated by the excitation coil [11]. In this case, the measurement result does not depend on the morphology of the dispersed ferromagnetic phase, and its volume fraction depends linearly on the saturation magnetization of the specimen (if the difference in the densities of the martensitic and austenitic phases is neglected).

### 4.4. Acoustic emission

A typical AE captured during the tensile test at $\dot{\varepsilon} = 5 \times 10^{-4}\ \text{s}^{-1}$ is shown in Fig. 8. There is a well defined AE response throughout the total loading time. Several AE pulses are observed after the yielding. A sudden increase in the AE activity occurred at about 2% of true equivalent plastic strain. After reaching the level of deformation corresponding to the change of hardening rate (at about 10% of true equivalent plastic strain) AE activity slightly decreased as it can be seen in the decreasing slope of the AE count. Most distinct AE pulses occur in the loading history at the same time as developing plastic deformation causes the martensitic transformation. The pulses were probably generated by twinning or slip accompanying the shear (displacive) transformation.

### 4.5. Thermal analysis

Mechanical response of AISI 301 steel is very sensitive to the strain rate. With the increasing strain rate yield stress increases, ultimate tensile strength decreases and elongation to fracture has a maximum at $\dot{\varepsilon} = 5 \times 10^{-3}\ \text{s}^{-1}$. The strong dependence on the strain rate is due to the coupling of thermo-mechanical behavior.

The temperature increase $\Delta T$ measured in the centre of specimen deformed at a strain rate $\dot{\varepsilon} = 5 \times 10^{-3}\ \text{s}^{-1}$, is illustrated in Fig. 9. Nearly the same values were obtained by integrating the formula:

$$dT(\sigma_{eq}, \varepsilon_{eq}^{pl}, f_m, x) = \frac{1}{\rho C_p}\left(0.9\ \sigma_{eq}\ d\varepsilon_{eq}^{pl} + \Delta H_m df_m - \lambda \frac{dT}{dx} dt\right) \qquad (4)$$

where $\rho$ is the density (8000 kg m$^{-3}$), $C_p$ the thermal capacity (500 J kg$^{-1}$ K$^{-1}$), $H_m$ the enthalpy of martensitic transformation (10,000 J kg$^{-1}$), $f_m$ the martensitic volume fraction and $\lambda$ the thermal conductivity of steel (16.2 W m$^{-1}$ K$^{-1}$).

The first term in brackets of Eq. (4) corresponds to the 90% of plastic deformation energy converted to the heating (curve adiabatic heating in Fig. 9), second term to the transformation heat and third term to the heat removal by thermal conduction. We as-
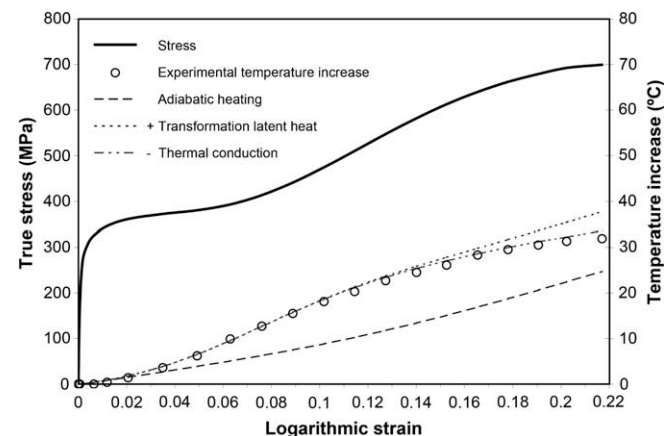
sumed the heat flux to jaws only, where the temperature was fixed to room temperature, e.g., $\Delta T(x = 0) = 0$.

In the case of slow strain rates ($<10^{-3}\ \text{s}^{-1}$), the heat removal prevails over the heat generation by the plastic deformation and the phase transformation so that the tensile test can be considered as isothermal (temperature increase $\Delta T \approx 0$).

In the case of higher strain rates ($>10^{-3}\ \text{s}^{-1}$), the transformation heat can be effectively separated and the volume fraction of deformation-induced martensite can then be determined.

## 5. Summary and conclusions

Experimental data presented in this paper provide comparison of the techniques characterizing the deformation-induced martensitic transformation in metastable austenitic steels. The results obtained on AISI 301 steel can be summarized as follows:

- In this low-nickel content austenitic steel, deformation-induced martensitic transformation starts only after low amount of plastic deformation (less than 2%). During straining, the volume fraction of $\alpha'$-martensite rapidly prevails over the volume fraction of $\varepsilon$-martensite.
- Accuracy of results obtained by diffraction methods is influenced by the type of radiation (penetration depth, sampled volume), experimental setup (angular range), etc. For the phase analysis from the inner volume of components, the most powerful technique is neutron diffraction, mainly due to the deep penetration of neutrons into investigated material (2–3 cm in steel). The sampled volume is therefore several orders of magnitude larger for neutron diffraction than for X-ray or EBSD. On the other hand, the information obtained by neutrons is averaged and integrated through the irradiated volume, as opposed to X-ray or EBSD. This fact indicates the relevance of combination of neutron diffraction method with other techniques which give the local information from near-surface layers, in order to examine the evolution of phase volume fraction within the studied material, or with the purpose of comparison of applied methods.
- *In situ* techniques such as magnetic induction measurement or AE monitoring are very precise in characterizing the kinetics of the deformation-induced martensitic transformation. Nevertheless, for the quantitative assessment of the martensitic volume fraction, these methods must be properly calibrated.

### Acknowledgements

### References

[1] Mangonon Jr L, Thomas G. The martensite phases in 304 stainless steel. Metall Trans 1970;1:1577–86.
[2] Suzuki T, Kojima H, Suzuki K, Hashimoto T, Ichihara M. An experimental study of the martensite nucleation and growth in 18/8 stainless steel. Acta Metall 1977;25:1151–62.
[3] Brooks JW, Loretto MH, Smallman RE. Direct observations of martensite nuclei in stainless steel. Acta Metall 1979;27:1839–47.
[4] Humbert M, Petit B, Bolle G, Gey N. Analysis of the $\gamma$–$\varepsilon$–$\alpha'$variant selection induced by 10% plastic deformation in 304 stainless steel at −60 °C. Mater Sci Eng A 2007;454–455:508–17.
[5] Sato K, Ichinose M, Hirotsu Y, Inoue Y. Effects of deformation induced phase transformation and twinning on the mechanical properties of austenitic Fe–Mn–Al alloys. ISIJ Int 1989;29:868–77.



**Fig. 9.** Temperature increase during the tensile test of AISI 301 steel tested at room temperature at $\dot{\varepsilon} = 5 \times 10^{-3}\ \text{s}^{-1}$.

[6] Mertinger V, Nagy E, Tranta F, Sólyom J. Strain-induced martensitic transformation in textured austenitic stainless steels. Mater Sci Eng A 2008;481–482:718–22.

[7] Timokhina I, Hodgson P, Pereloma E. Effect of alloying elements on the microstructure-property relationship in thermomechanically processed C–Mn–Si TRIP steels. In: De Cooman BC, editor. Proceedings of the international conference on TRIP-aided high strength ferrous alloys, Ghent, 2002. p. 153–7.

[8] Zhao L, Van Dijk NH, Brück E, Sietsma J, Van der Zwaag S. Magnetic and X-ray diffraction measurements for the determination of retained austenite in TRIP steels. Mater Sci Eng A 2001;313:145–52.

[9] Tavares SSM, Neto JM, Silva MR, Vasconcelos IF, Abreu HFG. Magnetic properties and α′ martensite quantification in an AISI 301LN stainless steel deformed by cold rolling. Mater Charact 2008;59:901–4.

[10] Baudry G, Pineau A. Influence of strain-induced martensitic transformation on the low cycle fatigue behaviour of stainless steel. Mater Sci Eng 1977;28:229–42.

[11] Radu M, Valy J, Gourgues AF, Le Strat F, Pineau A. Continuous magnetic method for quantitative monitoring of martensitic transformation in steels containing metastable austenite. Scripta Mater 2005;52:525–30.

[12] Dobmann G et al. Barkhausen noise measurements and related measurements in ferromagnetic materials. In: Birnbaum G, Auld BA, editors. Sensing for materials characterization, processing, and manufacturing. Djordjevic BB, Dos Reis H, editors. Topics on nondestructive evaluation series, vol. 1. American Society for Nondestructive Testing; 1998. p. 233.

[13] Tomáš I. Non-destructive magnetic adaptive testing of ferromagnetic materials. J Magn Magn Mater 2004;268:178–85.

[14] Niffenegger M, Leber HJ. Sensitivity of the magnetization curves of different austenitic stainless tube and pipe steels to mechanical fatigue. J Nucl Mater 2008;377:325–30.

[15] Heiple CR, Carpenter SH. Acoustic emission produced by deformation of metals and alloys — a review: part I. J Acoust Emission 1987;6:177–204.

[16] Heiple CR, Carpenter SH. Acoustic emission produced by deformation of metals and alloys — a review: part II. J Acoust Emission 1987;6:215–37.

[17] Wadley HNG, Furze D, Scruby CB, Eyre B. Effect of isothermal tempering on acoustic emission during ductile fracture on low alloy steel. Metal Sci 1979;13:451–62.

[18] Long QY, Zhu Z, Zhang XM, Li DF. Acoustic emission of martensitic transformation induced by strain during tensile testing in a Fe–Ni–C alloy. Scripta Metall Mater 1992;26:1095–100.

[19] Schaeffler AL. Constitution diagram for stainless steel weld metal. Metal Prog 1949;56:680. 680B.

[20] Scharam RE, Reed RP. Stacking fault energies of austenitic stainless steels. Metall Trans A 1975;6A:1345–51.

[21] Pecharsky KV, Zavalij PY. Fundamentals of powder diffraction and structural characterization of materials. 2nd ed. New York: Springer Science; 2008.

[22] Hill RJ. Howard CJ Quantitative phase analysis from powder diffraction data using the Rietveld method. J Appl Crystallogr 1987;20:467–74.

[23] Rodríguez-Carvajal J. An introduction to the program FullProf: a program for Rietveld refinement and profile matching analysis of complex powder diffraction patterns. 2001. <http://www.ill.eu/sites/fullprof/>.

[24] Stephens PW. Phenomenological model of anisotropic peak broadening in powder diffraction. J Appl Crystallogr 1999;32:281–9.

[25] Hoelzel M, Danilkin SA, Ehrenberg H, Toebbens DM, Udovic TJ, Fuess H, et al. Effects of high-pressure hydrogen charging on the structure of austenitic stainless steels. Mater Sci Eng A 2004;384:255–61.

[26] Hedström P. Deformation induced martensitic transformation of metastable stainless steel AISI 301. PhD thesis, Luleå University of Technology, Sweden; 2005.

[27] Shin HC, Ha TK, Chang YW. Scripta Mater 2001;45:823–9.

[28] Łuksza J, Ruminski M, Ratuszek W, Blicharski M. Texture evolution and variations of α-phase volume fraction in cold-rolled AISI 301 steel strip. J Mater Process Technol 2006;177:555–60.

[29] Humphreys FJ. Characterisation of fine-scale microstructures by electron backscatter diffraction (EBSD). Scripta Mater 2004;51:771–6.

[30] Gourgues-Lorenzon AF. Application of electron backscatter diffraction to the study of phase transformations. Int Mater Rev 2007;52:65–128.